Biophysical *Journal*
Article

Biophysical Society

In situ solid-state NMR study of antimicrobial peptide interactions with erythrocyte membranes

Kiran Kumar,[1,2] Mathew Sebastiao,[1,2] Alexandre A. Arnold,[1,2] Steve Bourgault,[1,2] Dror E. Warschawski,[1,3,*] and Isabelle Marcotte[1,2,*]

[1]Department of Chemistry, Université du Québec à Montréal, Montreal, QC, Canada; [2]Québec Network for Research on Protein Function, Engineering and Applications (PROTEO), Québec, QC, Canada; and [3]Laboratoire des Biomolécules, LBM, CNRS UMR 7203, Sorbonne Université, École Normale Supérieure, PSL University, Paris, France

ABSTRACT Antimicrobial peptides are promising therapeutic agents to mitigate the global rise of antibiotic resistance. They generally act by perturbing the bacterial cell membrane and are thus less likely to induce resistance. Because they are membrane-active molecules, it is critical to verify and understand their potential action toward eukaryotic cells to help design effective and safe drugs. In this work, we studied the interaction of two antimicrobial peptides, aurein 1.2 and caerin 1.1, with red blood cell (RBC) membranes using in situ ^{31}P and ^{2}H solid-state NMR (SS-NMR). We established a protocol to integrate up to 25% of deuterated fatty acids in the membranes of ghosts, which are obtained when hemoglobin is removed from RBCs. Fatty acid incorporation and the integrity of the lipid bilayer were confirmed by SS-NMR and fluorescence confocal microscopy. Leakage assays were performed to assess the lytic power of the antimicrobial peptides. The in situ perturbation of the ghost membranes by aurein 1.2 and caerin 1.1 revealed by ^{31}P and ^{2}H SS-NMR is consistent with membrane perturbation through a carpet mechanism for aurein 1.2, whereas caerin 1.1 acts on RBCs via pore formation. These results are compatible with fluorescence microscopy images of the ghosts. The peptides interact with eukaryotic membranes following similar mechanisms that take place in bacteria, highlighting the importance of hydrophobicity when determining such interactions. Our work bridges model membranes and in vitro studies and provides an analytical toolbox to assess drug toxicity toward eukaryotic cells.

SIGNIFICANCE Antimicrobial peptides are promising therapeutic agents to mitigate the global rise of antibiotic resistance. To develop drugs based on these peptides, the relevant forces dictating their membrane interaction mechanism need to be identified. In addition, their toxicity toward eukaryotic membranes should be assessed. Here we study the interaction of two antimicrobial peptides, aurein 1.2 and caerin 1.1, with erythrocytes by fluorescence leakage assays, confocal microscopy, and various NMR methods. The peptides interact with eukaryotic membranes following similar mechanisms that take place in bacteria, highlighting the importance of hydrophobicity when determining such interactions. Our work bridges model membranes and in vitro studies and provides an analytical toolbox to assess drug toxicity toward eukaryotic cells.

INTRODUCTION

Antimicrobial resistance affects the lives of many people around the world, and for this reason, the World Health Organization has recently published its first list of antibiotic-resistant bacteria that should be prioritized in the development of new treatments (1). New drug candidates with novel action mechanisms must be found urgently (2), and in this regard, antimicrobial peptides (AMPs) are a promising therapeutic alternative that could be subjected to advanced chemical engineering to become new antimicrobial drugs (3). The antimicrobial activity of AMPs involves different possible action mechanisms that cause bacterial cell death, including perturbation of the plasma membrane (4,5). Because these mechanisms are entirely distinct from those of current clinically used antibiotics, there is great interest in their development as therapeutic agents for antibiotic-resistant bacterial infections (6). Besides their direct cytotoxicity toward bacteria and fungi, several AMPs exhibit antiviral (7), antiparasitic (8), and anticancer properties (9). These biologically active

Submitted December 23, 2021, and accepted for publication March 7, 2022.
*Correspondence: marcotte.isabelle@uqam.ca or Dror.Warschawski@Sorbonne-Universite.fr
Editor: Timothy A. Cross.
https://doi.org/10.1016/j.bpj.2022.03.009

candidates are not only able to kill bacteria but also to modulate host immunity (10) because AMPs have evolved as integral components of strategic and carefully regulated mechanisms of immunity against infection (5).

In general, the outer surface of Gram+ and Gram− bacteria contains peptidoglycan and teichoic acids or lipopolysaccharides (11,12), each conferring a net negative charge. In addition, the outer leaflet of the lipid bilayer in bacterial membranes often contains zwitterionic phosphatidylethanolamine (PE) as well as negatively charged lipids such as phosphatidylglycerol and cardiolipin (13,14), promoting electrostatic interactions with cationic AMPs (15). In contrast, the outer leaflet of most mammalian cell membranes, including the erythrocyte membrane, mainly consists of zwitterionic phospholipids such as phosphatidylcholine (PC) and sphingomyelin (SM), as well as cholesterol (16). These fundamental differences between bacterial and eukaryotic membrane compositions should offer some specificity. Although many factors can influence this selectivity, including the molecular shapes of lipids and peptides (17), it has been proposed that charged peptides would preferentially interact with and affect the microbial membrane integrity with higher potency than with eukaryotic membranes (18,19). One major challenge is to identify AMPs for their potential therapeutic use and selectivity toward bacteria without affecting eukaryotic cells such as erythrocytes. Many studies have shown the potential of AMPs through their interaction with model membranes (20–23). However, model membranes have limited complexity and therefore overlook potentially important features of the cellular envelope. In this regard, in vivo studies are becoming more widespread, including in-cell solid-state NMR (SS-NMR) spectroscopy (24–26). In our previous study, aurein 1.2 (GLFDIIKKIAESF-NH_2) and caerin 1.1 (GLLSVLGSVAKHVLPHVVPVIAEHL-NH_2), natural AMPs isolated from the skin secretions of Australian tree frogs, were investigated (27–30). Their interaction with intact Gram+ and Gram− bacteria was studied by in vivo ^{2}H SS-NMR following specific deuteration of their membrane phospholipid acyl chains (24).

In this report, we investigated the action of these two cationic peptides on erythrocyte ghost membranes. The term "ghost" is used to describe the discoid bodies obtained after removal of hemoglobin from erythrocytes (31). As post-hemolytic remains of red blood cells (RBCs), their cell surface and membrane composition, including lipids, proteins, and other plasma membrane components, has been shown to be similar or even identical to that of intact RBCs (31,32). Hence, ghosts can be used to study the lipid phase, dynamics, and interactions in RBC membranes (33). Devoid of signal-perturbing hemoglobin or cytoplasmic phosphorus-containing molecules, ghosts are better suited for SS-NMR studies.

We first optimized and characterized the deuteration of erythrocyte ghosts with efficient incorporation of perdeuterated exogenous palmitic acid (PA-d_{31}) in their membranes. PA was chosen because saturated acyl chains with 16 carbons are the most abundant type of fatty acid (FA) chains in erythrocyte lipids (Fig. 5), and it is commercially available in its deuterated form. Similar labeling had been attempted in the past by Davis et al. (34), who intercalated PA-d_{31} molecules into lyophilized human erythrocytes and rehydrated them prior to NMR experiments. They obtained a 5% deuteration of the membranes and monitored the second moment of ^{2}H SS-NMR spectra as a function of temperature, showing no detectable phase transition down to 2°C, suggesting that PA-d_{31} molecules are present in all lipid regions of the membrane. In this work, we improved FA incorporation in the ghost membranes, reaching a level of 25% deuteration. We assessed changes in the lipid headgroup profile by ^{31}P solution NMR and in the FA chain composition by gas chromatography coupled to mass spectrometry (GC-MS). We also validated PA-d_{31} insertion by ^{2}H SS-NMR and GC-MS and membrane integrity by ^{31}P SS-NMR and confocal fluorescence microscopy.

After characterization of deuterated ghosts, we studied the effect of caerin 1.1 and aurein 1.2. Hemolytic and leakage assays were used to determine the lytic action of AMPs on erythrocyte and model membranes. Then ^{31}P and ^{2}H SS-NMR and confocal microscopy were employed to investigate the interactions of the peptides with erythrocyte ghost membranes. By performing these experiments at various lipid-peptide molar ratios, an overall picture of peptide interactions with erythrocyte membranes emerges. By determining the conditions under which these peptides perturb the membrane, their relative selectivity toward bacterial membranes is established.

MATERIALS AND METHODS

Materials

Caerin 1.1 and aurein 1.2 were synthesized by GenScript (Piscataway, NJ) with more than 95% purity. SM (egg, chicken), 1,2-dioleoyl-sn-glycero-3-phosphocholine (DOPC), 1,2-dioleoyl-sn-glycero-3-phosphoethanolamine (DOPE), 1,2-dioleoyl-sn-glycero-3-phospho-L-serine (DOPS), 1-palmitoyl-2-oleoyl-glycero-3-phosphocholine (POPC), 1-palmitoyl-2-oleoyl-sn-glycero-3-phosphoethanolamine (POPE), and 1-palmitoyl-2-oleoyl-sn-glycero-3-phospho-glycerol) (POPG) were obtained from Avanti Polar Lipids (Alabaster, AL). EDTA was purchased from Fisher Scientific (Fair Lawn, NJ), and PA-d_{31}, cholesterol, deuterium-depleted water, Triton X-100, FA methyl ester mix C4-C24, [16-[(7-nitro-2-1,3-benzoxadiazol-4-yl)amino] PA (NBD-PA), 1,1′-dilinoleyl-3,3,3′,3′-tetramethylindocarbocyanine 4-chlorobenzenesulfonate (FAST DiI), and all other solvents and chemicals were purchased from Sigma-Aldrich (Oakville, ON, Canada). Fresh horse RBCs packed 100% were purchased from Cedarlane Laboratories (Burlington, ON, Canada). Deionized 18.2 MΩ.cm Milli-Q water was used in all experiments (Millipore-Sigma, Oakville, ON, Canada).

Ghost sample preparation and labeling

Ghosts were prepared as described previously (32) with some modifications. Concentrated horse RBCs were suspended in a 40-mL round-bottom centrifugation tube with isotonic HEPES buffer (20 mM HEPES, 150 mM NaCl (pH 7.4)) and centrifuged at 500 × g for 5 min at 4°C. Supplementary washes (2–3) in the same buffer were carried out until the supernatant became clear.

After the final wash, the pellet was resuspended in 20 mL hypotonic HEPES buffer (20 mM HEPES (pH 7.4)) and centrifuged at 25,000 × *g* for 40 min at 4°C (rotor JA-20, Beckman Coulter). The supernatant was removed, and the pellet was transferred into new centrifuge tubes, leaving behind the "red button" that contained proteases. Additional washes (3–4) with the same buffer were carried out until the pellet became white.

A 0.5 mM Triton X-100/0.25 mM PA-d_{31} mixed micelle (35) solution in isotonic buffer was prepared in a sealed glass vial with three freeze (−20°C)/thaw (95°C) cycles. The white ghost pellet was then resuspended in 320 mL isotonic buffer to which 80 mL of the mixed micelle solution was added and incubated for 15 min at 37°C. The mixture of ghosts and micellized PA-d_{31} was then centrifuged at 25,000 × *g* for 20 min at 4°C in different 20-mL aliquots. The excess detergent was washed away by centrifugation in isotonic buffer twice more at 25,000 × *g* for 20 min at 4°C. The ghost pellets were pooled in a 1.5-mL Eppendorf tube and centrifuged at 20,000 × *g* for 20 min at 4°C. The pellet was then washed in an isotonic buffer prepared with deuterium-depleted (DD) water, first at 20,000 × *g* for 20 min at 4°C and then at 100,000 × *g* and 4°C for 20 min. This concentrated pellet was collected and stored at 4°C prior to the experiments. To calculate the lipid-to-peptide ratios, the lipid concentration after ghost preparation was determined by high-resolution ^{31}P solution NMR after lipid extraction, as described in the Supporting material (Fig. S1).

Preparation and labeling of liposomes

Multilamellar liposomes (MLVs) were prepared using the film method as described by Warschawski et al. (36). Lipid powders (including cholesterol and labeled PA-d_{31}) were dissolved in 2:1 methanol/$CHCl_3$ solution and dried under a nitrogen stream. Residual organic solvent in lipid film was removed by high vacuum for at least 2 h. The film was then hydrated with a physiologically relevant buffer (20 mM HEPES, 150 mM NaCl (pH 7.4)) in DD water. Lipid dispersion was vortexed and freeze-thawed 5–8 times (10 min at −20°C followed by 10 min at 55°C) and transferred directly into a 4-mm rotor.

Microscopy sample preparation

Ghosts 1% (v/v) were labeled with FAST DiI (1/1000) using 10 rpm longitudinal rotation for 1 h at 37°C and then pelleted at 16,000 × *g* for 15 min. The pellet was resuspended in 500 μL HEPES buffer, transferred to Sarstedt eight-well microscopy slides (300 μL), and left to stand for 30 min to allow ghost immobilization. NBD-PAs were incorporated into ghosts along with PA or PA-d_{31}as described above. After addition of an appropriate amount of AMPs, calcein influx experiments were performed by adding 0.5 mM calcein directly to 1% (v/v) ghosts. Images were acquired using a Nikon confocal microscope with a 60× oil immersion lens and processed using ImageJ software.

Lipid and FA profile

The lipid profile was determined following the procedure of Laydevant et al. (37). Lipid extraction was performed in triplicate using the Folch protocol (38), and freeze-dried sample weights were measured using a XP205 Mettler Toledo analytical balance (up to 0.01 mg readability). Then samples were dissolved in a biphasic solution composed of 200 μL CD_3OD, 500 μL $CDCl_3$ (organic phase), and 50 μL of 200 mM EDTA (acid form) at pH 6.00 ± 0.04 (aqueous phase). Solution NMR spectra were acquired using a 600-MHz Avance III HD (Bruker, Milton, ON, Canada) spectrometer equipped with a 5-mm broad-band probe operating at 243 and 600 MHz for ^{31}P and ^{1}H, respectively. 1D ^{31}P NMR spectra were obtained with ^{1}H decoupling and employed 384 scans at 25°C with a 10-s relaxation delay to obtain quantitative data. To identify the lipid profile, commercially available pure synthetic lipid (DOPC, 1,2-dioleoyl-sn-glycero-3-phosphoethanolamine, 1,2-dioleoyl-sn-glycero-3-phospho-L-serine, and SM) solutions were spiked in the sample. Remaining ambiguities were resolved by 2D ^{31}P-^{1}H TOCSY (total correlation spectroscopy) NMR experiments as described by Balsgart et al. (39) at 25°C with 12,000 data points in the direct dimension and 200 data points in the indirect dimension, a repetition delay of 2 s, and a TOCSY mixing time of 70 ms. The acquisition time in the direct dimension was 2.8 s for a total acquisition time of 22 h per 2D spectrum.

Samples used for solution NMR analyses were then recovered and prepared for FA analysis by GC-MS. Briefly, samples were filtered, and then transesterification was carried out in 2 mL of H_2SO_4 (2% in methanol) and 0.8 mL of toluene for 10 min at 100°C.The GC-MS analyses were carried out as described by Laydevant et al. (37) using a polar HP-5MS column (30 m length × 250 μm diameter × 0.25 μm film thickness). The injection volume was 1 μL, and the oven temperature was programmed to heat at 140°C for 5 min, followed by a 4°C/min ramp up to 300°C, prior to electron ionization and detection with a quadrupole MS. Data acquisition and processing were performed with Chemstation software.

Hemolysis assay

The hemolytic activity of the AMPs was determined by measuring the hemoglobin released from horse RBCs as described previously (19). A volume of 500 μL of packed RBCs was centrifuged at 500 × *g* and 4°C for 5 min to recover the erythrocytes, and the supernatant was removed. The pellet was subsequently washed three times with 10 mL of phosphate-buffered saline (PBS) isotonic buffer to obtain a clear supernatant. The 30-μL erythrocyte pellet was resuspended in 270 μL of a solution containing the AMPs at the desired concentration (diluted in PBS buffer) to obtain a final concentration of 5% RBCs (v/v) containing about 5–10 × 10^8 cells/mL. The sample was incubated at 37°C for 1 h. The PBS buffer and 1% Triton X-100 solution were used as negative (A_0) and positive (A_{100}) controls, respectively. After 500 × *g* centrifugation for 5 min, the hemoglobin concentration in the supernatant (diluted to 2% RBCs in PBS buffer) was determined using an ultraviolet-visible spectrophotometer by monitoring the optical density at 576 nm. The percentage of hemolysis was calculated with the following equation:

$$\%hemolysis = \frac{A - A_0}{A_{100} - A_0} \times 100 \quad (1)$$

Carboxyfluorescein leakage assays

Large unilamellar vesicles (LUVs) that mimic erythrocyte and bacterial membranes were prepared for the carboxyfluorescein (CF) leakage experiments by encapsulating CF into LUVs. About 20 mM lipids were rehydrated in a buffer (20 mM HEPES (pH 7.4)) containing 46 mM CF, and MLVs were prepared using five freeze-thaw cycles and a 5-min vortex step each time. LUVs were obtained by extruding the MLV suspension through a polycarbonate filter with 100-nm pores (Avanti Polar Lipids). The CF-containing vesicles were separated from non-entrapped CF using a Sephadex G25 Fine (20 × 80 mm) size-exclusion chromatography column eluted with buffer. The lipid concentration of separated LUVs was determined by a phosphorus assay in triplicates. 12.5 μL of the liposome suspension of each lipid system was resuspended in 87.5 μL of solution containing AMPs at the desired concentration (diluted in HEPES buffer), and the sample was incubated at 37°C for 1 h. The buffer and 1% Triton X-100 were used as negative (F_0) and positive (F_{100}) controls, respectively. The percentage of CF released was measured using a microplate reader set at $\lambda_{emission} = 517$ nm and $\lambda_{excitation} = 495$ nm. The percentage of leakage (%L) was calculated with the following equation:

$$\%L = \frac{F - F_0}{F_{100} - F_0} \times 100 \quad (2)$$

SS-NMR and spectral moment analysis

^{31}P and ^{2}H SS-NMR spectra were acquired using a Bruker Avance III-HD wide-bore 400 MHz spectrometer with respective resonance frequencies of 162 and 61.5 MHz. Static ^{31}P SS-NMR spectra were obtained using a phase-cycled Hahn echo pulse sequence (40) with high-power (50 kHz) ^{1}H decoupling during acquisition. Using a 90° pulse length of 3 μs and an interpulse delay of 35 μs, data were collected using 1024 points with a recycle delay of 3 s and a total of 14,000 scans per spectra, amounting to 12 h of acquisition. Magic-angle spinning (MAS) ^{2}H SS-NMR experiments were carried out using a 10-kHz spinning frequency and a phase-cycled quadrupolar echo sequence (41) with 100,000 data points acquired with a 90° pulse length of 4 μs, a rotor-synchronized interpulse delay of 96 μs, and a recycle time of 500 ms. A total of 44,000 scans per spectra were acquired for 8 h. A line broadening of 100 Hz was applied to all spectra, and the ^{31}P chemical shift anisotropy (CSA) was determined by line fitting using Bruker Topspin 4.0.6 and Sola (Solid Lineshape Analysis) software.

^{2}H spectral moment analysis was performed using MestRenova software v.6.0 (Mestrelab Research, Santiago de Compostela, Spain). Second spectral moments, M_2, were calculated using Eq. 3 (41),

$$M_2 = \omega_r^2 \frac{\Sigma_{N=0}^{\infty} N^2 A_N}{\sum_{N=0}^{\infty} A_N} = \frac{4\Pi^2 \nu_Q^2}{5} \langle S_{CD}^2 \rangle \qquad (3)$$

where ω_r is the angular spinning frequency, N is the side band number, A_N is the area of each side band obtained by spectral integration, S^2_{CD} is the mean square order parameter, and ν_Q is the static quadrupolar coupling constant equal to 168 kHz for a C-D bond in acyl chains (42). The M_2 value provides a quantitative description of the membrane lipid ordering and is particularly sensitive to the gel-to-fluid phase transition. Despite using DD water, a residual HDO peak remains, which accounts for 10%–15% of the total ^{2}H NMR spectral intensity. This residual peak is excluded from the spectral moment calculation.

RESULTS

Incorporation of FAs into erythrocyte ghost membranes

Plasma membranes of RBCs are significantly different from those of bacteria. Notably, they contain 30%–40% cholesterol, and their phospholipid acyl chains show a higher degree of ordered phase than those of fluid bacterial membranes. Although erythrocyte ghost membranes have been labeled previously with deuterated FAs (33), here we show that the labeling can be improved to facilitate study of peptide-membrane interactions. A first set of experiments was performed to optimize the incorporation conditions of PA-d_{31} into ghost membranes. Optimal insertion was achieved by incubating ghosts in the presence of Triton X-100/PA-d_{31} mixed micelles. In the presence of ghost membranes, these micelles are in a dynamic association-dissociation equilibrium whose kinetics depend on temperature, pressure, and concentration (43). They were diluted so that the concentration of Triton X-100 was decreased to 0.1 mM during the incorporation step; i.e., well below the critical micelle concentration of Triton X-100 (0.23 mM) (35). Nonionic surfactants such as Triton X-100 tend to undergo slow dissociation during which exchange of FAs between the mixed micelles and phospholipid bilayers occurs. Because FA incorporation in the bilayer is thermodynamically favorable, the exchange equilibrium is shifted toward the bilayer, and the ghost membrane can thus be efficiently ^{2}H labeled (44,45). Although a full quantitative understanding of this process is beyond the scope of this work, the relative partitioning of PA versus Triton X-100 in the membrane is likely to be a key factor for successful labeling. Indeed, the partition coefficient of PA is two orders of magnitude higher than the one of Triton X-100 in PC membranes (103×10^3 M^{-1} for PA versus 3×10^3 M^{-1} for Triton X-100) (46,47). PA is thus favorably inserted into the membrane, and the residual detergent, which favorably remains in the buffer, can be removed by a series of washing steps.

At a concentration of 0.1 mM, the surfactant is harmless to the cell membranes, as demonstrated elsewhere (35,48). This is supported by the ^{31}P SS-NMR spectrum (Fig. 1 *B*), which is characteristic of an intact lamellar lipid phase and comparable with PC/SM/cholesterol/PA-d_{31} (5:3:7:5 molar ratio) model RBC membranes (Fig. 1 *C*) as well as unlabeled ghosts (Fig. 1 *A*). The ^{31}P CSA value of deuterated ghosts is in good agreement with that of unlabeled ghosts and model membranes as well as previous studies of lipid bilayers (49) (Fig. 1). As shown in Fig. 2, *A*–*C*, the integrity of the RBC ghost morphology is confirmed by confocal fluorescence microscopy. A z stack of multiple optical sections also reveals that ghosts retain the biconcave disc shape of RBCs (Fig. 2 *D*).

To ensure that the ghost membranes were effectively labeled, ^{2}H SS-NMR spectra were recorded (Fig. 1 *D*) using MAS, providing a high signal-to-noise (S/N) ratio in a few hours, similarly to bacteria (4). The presence of spinning side bands proves that a significant amount of deuterated FAs is no longer incorporated in fast tumbling objects such as micelles but, rather, found in an environment with restricted motion, such as a membrane bilayer. The ^{2}H spectrum is very similar to the one obtained for a model membrane with the same lipid composition (Fig. 1 *E*), confirming that PA-d_{31} is indeed in a membrane environment. Incorporation of PA is supported by fluorescence microscopy images, which locate NBD-PA, a fluorophore structurally similar to PA-d_{31}, in the ghost membranes (Fig. 2, *C* and *D*).

Incorporation of PA-d_{31} into ghost membranes was ascertained by comparing the FA ordering in labeled ghosts and in model membranes with increasing composition complexity. The M_2 from ^{2}H SS-NMR spectra was determined at several temperatures. Indeed, if PA-d_{31} is incorporated in the ghost membranes, then the evolution of its ^{2}H M_2, which reflects the fluidity of the membrane, with temperature is expected to be similar to the one in a model membrane that closely matches the lipid composition of ghosts (Fig.1, *D* and *E*). As shown in Fig. 3, the ordering of PA-d_{31} in DOPC/cholesterol (Chol)/PA-d_{31} and, to a lesser extent, in DOPC/PA-d_{31} shows a reduction with

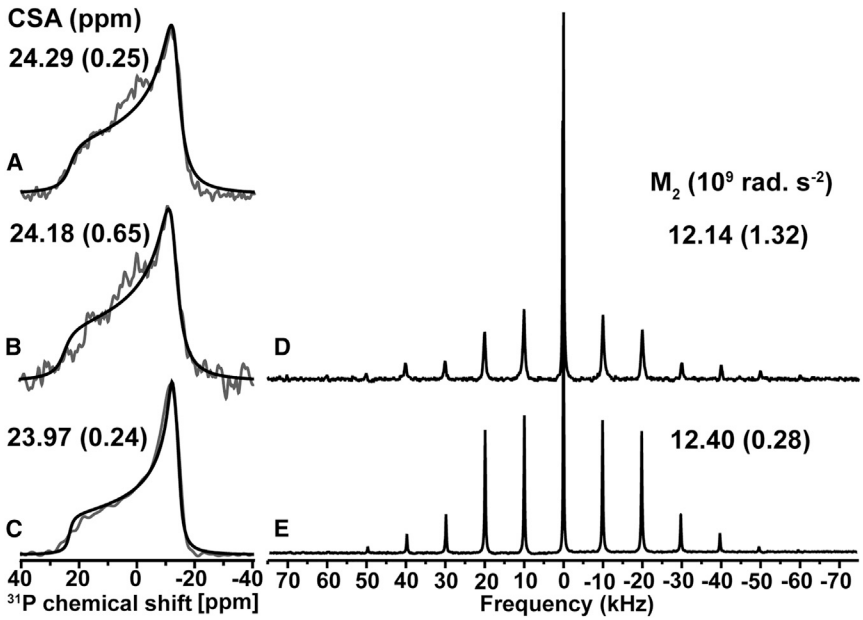

FIGURE 1 NMR spectra of ghosts and model membranes. (*A–C*) Static ^{31}P SS-NMR spectra with spectral fitting and average CSA of (*A*) unlabeled, (*B*) deuterated ghosts, and (*C*) DOPC/SM/Chol/PA-d_{31} (5:3:7:5) model membranes. (*D* and *E*) ^{2}H SS-NMR spectra with MAS (10 kHz) of (*D*) deuterated ghosts and (*E*) DOPC/SM/Chol/PA-d_{31} (5:3:7:5) model membranes with M_2 values. All spectra were recorded at 293 K. The residual HDO peak in deuterium-labeled ghosts accounts for 10%–15% of the total ^{2}H intensity and is not integrated in the M_2 calculation.

increasing temperature. Addition of sphingomyelin appears to cancel this temperature dependence. Interestingly, PA-d_{31} ordering in labeled ghosts as a function of temperature closely follows the one of the model membranes whose composition is the closest to erythrocyte membranes (DOPC/SM/Chol/PA-d_{31}) (Fig. 3). The temperature dependence of ^{2}H M_2 values thus appears to confirm incorporation of FAs into the ghost membrane. Moreover, as shown by ^{31}P SS-NMR and confocal fluorescence microscopy, the membrane integrity of these labeled ghosts is preserved.

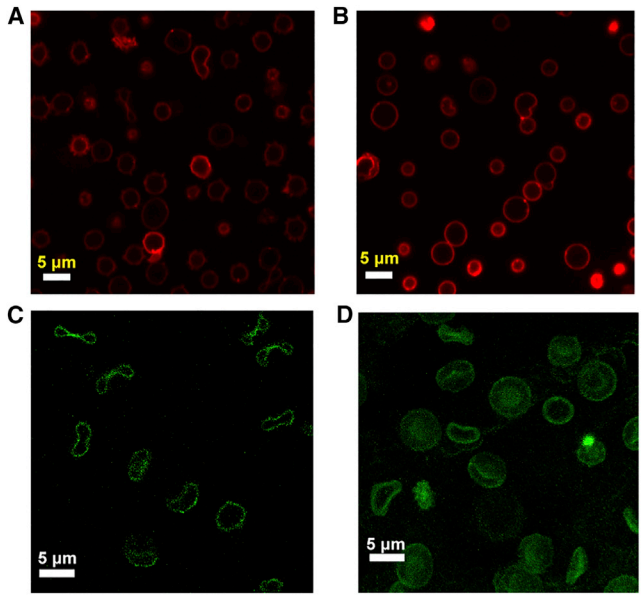

FIGURE 2 Characteristic confocal fluorescence microscopy images of prepared erythrocyte ghosts, indicating that the membranes are intact, incorporation of PA-d_{31} does not appreciably alter the overall morphology, and PA molecules are evenly dispersed throughout the plasma membrane. (*A*) Non-deuterated ghosts labeled with the lipophilic tracer FAST DiI (red). (*B*) Ghosts with PA-d_{31} incorporated into the plasma membrane, labeled with the lipophilic tracer FAST DiI (red). (*C*) Deuterated ghosts prepared in the presence of fluorescent NBD-PA (green). (*D*) Z projection of multiple planes of the deuterated ghosts prepared with fluorescent NBD-PA (green). Scale bars are 5 µm. To see this figure in color, go online.

Lipid composition of erythrocyte and ghost membranes

To characterize possible alterations to the lipid profile upon ^{2}H-labeling of RBC ghost membranes, phospholipids were identified and quantified using 1D ^{31}P solution NMR after lipid extraction (Fig. S2). ^{31}P resonances of the main phospholipids (PE, PC, SM, and PS) were identified by comparison with the chemical shifts of standards and the literature (37). Lipid proportions were determined by integrating those resonances and are reported in Table S1.

To identify other lipids, in particular ether-linked phospholipids, we used a 2D ^{1}H–^{31}P TOCSY experiment in solution NMR (39), as shown in Fig. 4. All ^{1}H and ^{31}P chemical shifts are reported in Table S1, and two ^{31}P lipid columns, at −0.75 and 0.18 parts per million (ppm), showed a marked shift of their g_2 glycerol proton from 5.05 ppm to 4.97 ppm. We assign this shift to originate from a change in linkage from an ester to an ether group in ether PC and ether PE, the additional oxygen in ester-linked lipids further deshielding the glycerol protons (50). One last ^{31}P lipid column, at 0.22 ppm, was not assigned from the 1D ^{31}P solution NMR spectra. Its proton NMR pattern is similar to that of SM, and we assigned it to dihydrosphingomyelin (DHSM), which is compatible with a previous assignment in a different context (51). Although ether PC is only ∼20% of

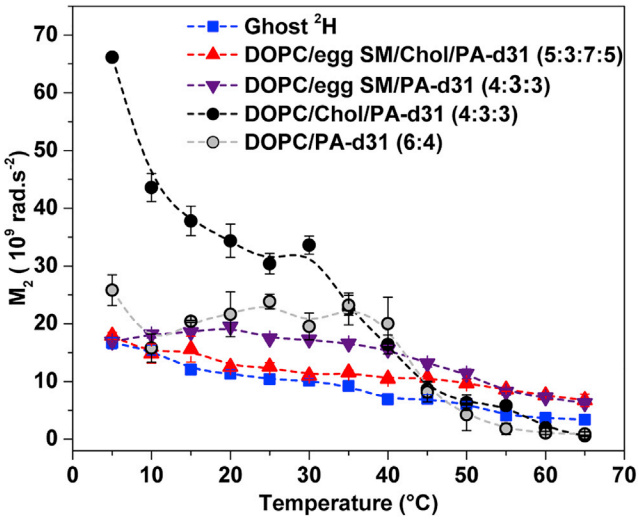

FIGURE 3 Membrane fluidity of model membranes and ghosts incorporating PA-d_{31}, as a function of temperature, as reported by the second spectral moment, M_2, calculated from ^{2}H SS-NMR spectra, error bars correspond to standard deviations of three replicates. The similarity between the M_2 values obtained for labeled ghosts and model membranes with the closest lipid composition is a strong indication that PA-d_{31} is incorporated in the ghost membrane. To see this figure in color, go online.

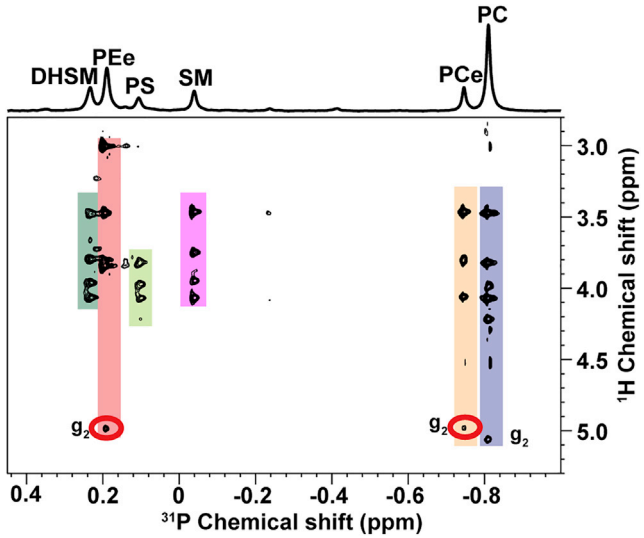

FIGURE 4 2D ^{1}H-^{31}P TOCSY spectrum of RBC membrane phospholipids extracted by the Folch method and solubilized in CD_3OD:$CDCl_3$ solution to which a small amount of EDTA aqueous solution was added. This eliminates ionic species from the organic phase and improves lipid solubility (see Materials and methods for more details). To see this figure in color, go online.

the total PC lipids, we note that around 60% of SM lipids are DHSM and that almost all of PE lipids are actually ether PE.

After determination of lipid proportions by ^{31}P solution NMR, the FA proportions were determined by GC-MS after lipid hydrolysis. Complete and unambiguous quantification of the phospholipid profile of native horse RBCs, ghosts, and ^{2}H-labeled ghosts is summarized in Fig. 5 and shows that the membrane phospholipidic profile is in good agreement with the literature (52) and that it was unaltered during preparation of ghosts and incorporation of deuterated FAs. As determined by GC-MS and shown in Fig. 5, incorporation of PA-d_{31} was highly successful because it represents about 25% of the total FA chains in the ghost membrane. Consequently, a change in membrane fluidity is expected because the labeled ghosts contain about 65% of saturated FAs compared with 50% in native RBCs. The incorporation of PA-d_{31} together with protonated unsaturated FAs, such as oleic acid (C18:1), could help reestablish a more natural saturated/unsaturated FA ratio, as done with bacteria (24,53). However, considering the low ^{2}H NMR S/N ratio obtained with ^{2}H-labeled ghosts, addition of protonated FAs would reduce the sensitivity of the ^{2}H SS-NMR experiments, prohibiting this approach. The lower S/N ratio obtained with ^{2}H-labeled ghosts compared with ^{2}H-labeled bacteria (24,54) can be explained by the impossibility to prepare ghost samples with sufficient concentration through centrifugation even at 100,000 × g. Moreover, exogenous PA-d_{31} is used by bacteria for phospholipid synthesis, increasing membrane labeling. The NMR and GC-MS results show that ghosts can be labeled and enable membrane-peptide interaction studies by SS-NMR.

Effect of AMPs on erythrocyte membranes

Leakage experiments

Perturbation of phospholipid bilayers by AMPs can occur through various processes (18), most notably via a carpet-like mechanism or pore formation (55). At different stages of these processes, membrane disruption, in the case of RBCs, can lead to hemoglobin leakage, which can readily be monitored. The lytic activity of caerin 1.1 and aurein 1.2 on actual RBCs and model membranes has been determined previously (56–60). We measured the lytic activity of these peptides on RBCs, reporting peptide and lipid concentrations, enabling calculation of lipid/peptide (L/P) molar ratios at which lysis occurs. This additional information allows direct comparison with our leakage assays on RBC ghosts and erythrocyte models with a membrane composition (POPC/SM/Chol) closer to RBCs than reported previously.

As shown in Fig. 6 *A*, although caerin 1.1 seems to have a higher lytic potency on RBCs than aurein 1.2 (with a higher hemolytic activity and a plateau at a higher L/P molar ratio), differences are much smaller than in model membranes (Fig. 6, *B* and *C*) and fall within the experimental uncertainty. The threshold concentrations and L/P molar ratios at which membrane perturbation occurs are reported in Table 1. Characteristic literature values are also indicated to compare our results with those of previously published antimicrobial assays. By examining the results in Table 1, it appears that caerin systematically shows a higher permeabilization potency than aurein in all membrane systems. Our results show that caerin has lower minimum inhibitory concentrations (MICs) on *Escherichia coli* and *Bacillus subtilis*

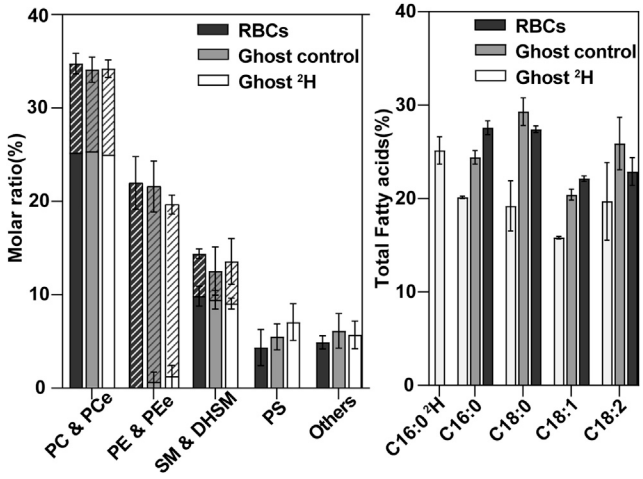

FIGURE 5 Phospholipid headgroup and fatty acyl chain profile of horse RBCs, ghosts, and deuterated ghosts obtained from ^{31}P NMR and GCMS analyses, respectively, error bars correspond to standard deviations of at least three replicates. Crosshatched areas correspond to ether-linked or DHSM lipids. Complete data are reported in Tables S1 and S2.

and higher L/P molar ratios at which 50% of RBCs or membranes are lysed (LR50) on model membranes and, to a lesser extent, RBCs. It is noteworthy that lysis of 50% of the RBCs occurs at L/P molar ratios that are one to two orders of magnitude lower than in the model eukaryotic (POPC/SM/Chol) or bacterial (POPE/POPG) membranes. This result indicates that RBCs are significantly more resistant than model membranes to AMP-induced lysis and highlights the importance of assessing AMP activities on intact cells.

Working with actual RBCs enables us to elucidate the action mechanism of AMPs on these eukaryotic membranes and address the question of their selectivity toward bacterial membranes. Indeed, a striking difference is observed for aurein, for which eight times more peptide is required to achieve 50% lysis of the bacterial model membranes compared with model RBC membranes despite the negative charge of the former. On the other hand, caerin shows a strikingly lower selectivity with 50% lysis of both model membranes at roughly the same L/P ratios (126:1 and 105:1). One might thus expect aurein to show a higher toxicity than caerin for RBCs. However, the LR50 values of both peptides on RBCs are very similar (2.6:1 (0.2) and 3.2:1 (0.2) for aurein and caerin, respectively), and no significant differences in the concentrations at which the peptides lyse 10% of RBCs are observed.

To quantify the selectivity of both AMPs toward bacteria and, therefore, their potential toxicity, the therapeutic index (TI) was calculated. This index is defined as the ratio between the minimum hemolytic concentration (MHC) and the MIC, which we obtained in our previous work on bacteria (24). A large TI value indicates higher selectivity toward a given bacterium. Table 1 shows that the calculated TI values for aurein 1.2 and caerin 1.1 are low, revealing poor selectivity of both peptides toward bacteria, a tendency observed previously (56,61). Both peptides seem to be more selective to the Gram+ *B. subtilis*, with TI values three times the ones obtained for *E. coli*, although differences between the two peptides might be obscured by the poor accuracy of MHC values. Further chemical modifications would be required to enhance the selectivity of these AMPs toward bacteria to reduce their cytotoxicity. However, it is difficult to compare TI values between different studies because they are determined with various assays and different blood-resident cells (19).

SS-NMR experiments

To investigate the interaction of AMPs with erythrocyte membranes, perturbation of the phospholipid headgroups

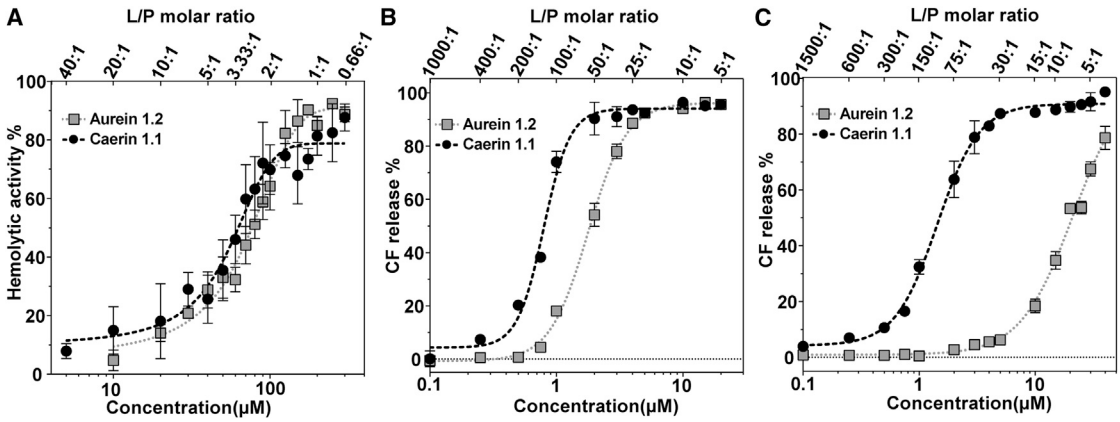

FIGURE 6 Lytic activity of AMPs on erythrocytes and model membranes. (*A*) hemoglobin leakage of RBCs with a phospholipid concentration of 200 μM, (*B*) CF leakage of POPC/SM/Chol LUVs with a lipid concentration of 100 μM, and (*C*) CF leakage of POPE/POPG with a lipid concentration of 150 μM. Results are presented as the mean of triplicate assays, error bars are the standard deviations of at least three replicates. Dashed and dotted lines correspond to the best fit to a sigmoidal curve. To compare the relative effects of the AMPs on whole cells and lipid model membranes, molar L/P ratios are indicated. Details of the experimental estimation of RBC lipid concentration are presented in the Supporting material. For comparison with other works, data presented as a function of L/P weight ratios are also reported in the Supporting material (Fig. S3).

TABLE 1 Comparison of the effects of the AMPs on red blood cells (RBCs), model RBCs, and bacterial membranes as well as different bacteria

	RBCs	POPC/SM/Chol	POPE/POPG	RBCs	*E. coli*		*B. subtilis*	
AMPs	LR50	LR50	LR50	MHC (μM)	MIC (μM)	TI	MIC (μM)	TI
Aurein 1.2	2.6:1 (0.2)	54.3:1 (2.4)	7.2:1 (0.1)	15.8 (2.7)	68	0.23 (0.04)	20	0.79 (0.13)
Caerin 1.1	3.2:1 (0.2)	124.7:1 (2.0)	100.3:1 (10.2)	12.1 (3.6)	39	0.31 (0.09)	12	1.00 (0.30)

The leakage assays were performed on intact RBCs. The minimum hemolytic concentration causing 10% leakage of RBCs (MHC) and the lipid-to-peptide molar ratio at which 50% leakage occurs (LR50) are obtained by fitting of the leakage assays shown in Fig. 6 *A*. MIC, minimum inhibitory concentration (24); TI, therapeutic index.

and deuterated hydrophobic core of RBC ghosts were studied by static ^{31}P and MAS ^{2}H SS-NMR, respectively (Fig. 7). The ^{31}P SS-NMR experiments shown in Fig. 7 were carried out on non-deuterated ghosts to approach native conditions and keep the samples as fresh as possible; however, experiments performed with deuterated ghosts did not reveal significant differences (Table S3; Fig. S4).

As seen in Fig. 7, a narrow peak appears on the ^{31}P NMR spectrum at ~0 ppm when the proportion of aurein 1.2 is increased. This type of central peak has been discussed by Yang et al. (62) and can result from phospholipids in rapidly reorienting small objects, such as micelles, or from phospholipids in high-curvature membrane regions, such as buds, cubic phases, or toroidal pores. Those cases differ by their relaxation times and line widths, with the narrowest lines being assigned to micelles and the broader ones to high-curvature regions.

In the case of aurein, the breadth of this central peak (~1000 Hz) gradually decreases to a value of 200 Hz, consistent with formation of micelles that end up being released from the membrane, leading to a sharp peak at a 1.7:1 L/P molar ratio. Interestingly, the CSA value of the remaining lamellar phase is unchanged up to an L/P ratio of 3:1 (Table S4). Simultaneously, the PA dynamics in the hydrophobic core increases, as revealed by the decrease in the spinning side-band intensities on the ^{2}H SS-NMR spectra and the concomitant decrease in M_2 values (Figs. 7 *A* and 8 *B*). We had reported an increase in M_2 in the early stages of the interaction of aurein with *B. subtilis* membranes (24). Thus, differences between the first stages of aurein association with Gram+ bacteria and ghosts cannot be excluded.

The behavior of caerin is significantly different compared with aurein. As the peptide concentration increases, an isotropic peak intensifies on the ^{31}P spectra and remains broad (full width at half height of 1000–1500 Hz) at all concentrations (Figs. 7 *B* and 8 *B*), compatible with phospholipids in high-curvature membrane regions. Interestingly, and in contrast with the effect of aurein, the PA dynamics with caerin concentration evolve in two stages, as revealed by ^{2}H SS-NMR (Fig. 8; Table S4). In a first stage, the dynamics slightly diminish, as seen by the increase in M_2 from 9.9 with no caerin (not shown on logarithmic scale) to 11.3×10^9 rad s^{-2} when caerin concentration is increased up to an L/P molar ratio of 6:1. When the peptide concentration is raised further, lipid dynamics increase to return to the initial M_2 value and remain constant up to the maximum L/P ratio studied (3:1). We should point out that this behavior is different from the one we observed in *B. subtilis* bacterial membranes (24) and could

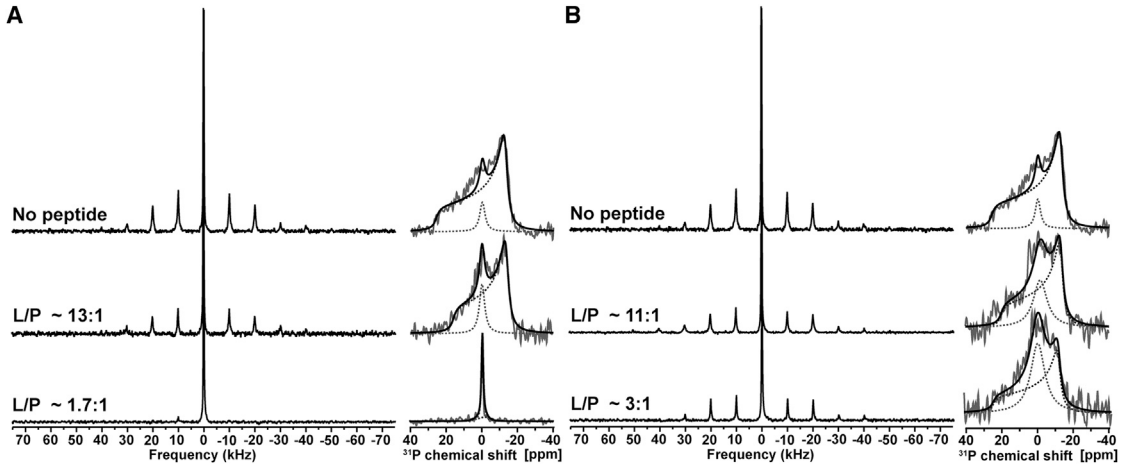

FIGURE 7 ^{2}H MAS (10 kHz) SS-NMR spectra and ^{31}P static SS-NMR spectra of ghosts, acquired at 293 K, with different concentrations of AMPs. (*A*) aurein 1.2 and (*B*) caerin 1.1. The corresponding lipid-to-peptide molar ratios (L/P) are indicated. ^{31}P static and ^{2}H MAS SS-NMR spectra were obtained with unlabeled and deuterated ghosts, respectively. For ^{31}P SS-NMR spectra, dotted lines represent spectral fitting of the broad anisotropic component and the central peak (numerical values are shown in Tables S3 and S4).

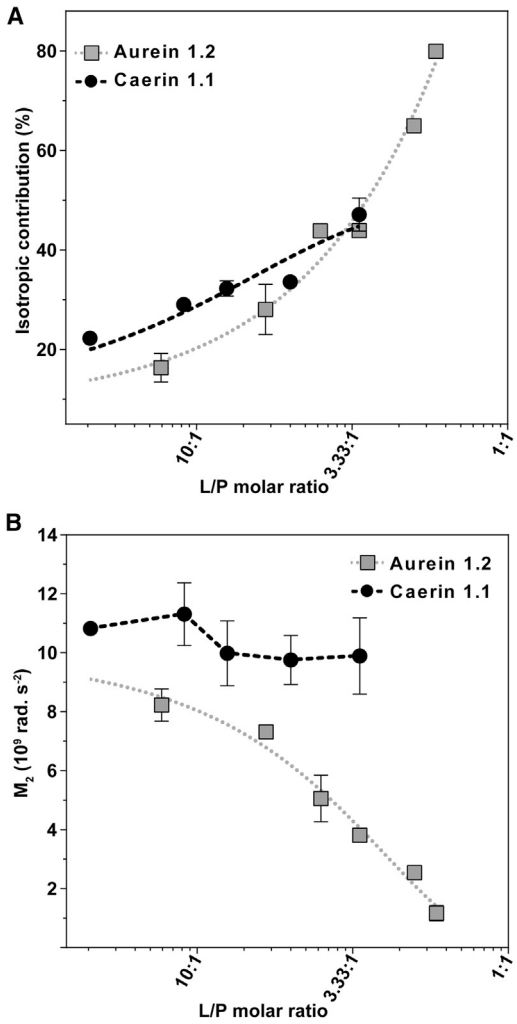

FIGURE 8 Effect of aurein 1.2 and caerin 1.1 on erythrocyte ghosts as a function of the peptide-to-lipid (P/L) molar ratio, at 293 K. (*A*) Isotropic contribution to the ^{31}P SS-NMR spectra of unlabeled ghosts. (*B*) M_2 of deuterated ghosts determined from ^{2}H MAS SS-NMR spectra. All error bars correspond to standard deviations of at least three replicates. Phospholipid concentrations range from 4 to 9 mM. Dashed and dotted lines correspond to the best fit to a sigmoidal curve or a simple guide to the eye when fitting was not possible (caerin 1.1, B).

indicate subtle differences in the pore formation molecular mechanism between the two cell types.

Microscopy experiments

Confocal microscopy results further support our SS-NMR findings. With FAST DiI and NBD-PA labeling, labeled and unlabeled ghosts appear to be destroyed by aurein 1.2 at an L/P molar ratio of 1.7:1 (Figs. 9, center column, and S5). Aurein 1.2, with its relatively short 13-amino-acid sequence, has been shown to perturb bacterial and mammalian model membranes through a carpet-like mechanism (60). Our SS-NMR and fluorescence microscopy results support a similar action toward RBC ghosts.

Caerin 1.1, with its 25-amino-acid sequence that can span the membrane, triggers hemolysis at lower concentrations than aurein (Fig. 6). The fluorescence confocal microscopy images in Fig. 9, recorded using FAST DiI entrapped in ghosts, show intact membranes in the presence of caerin at concentrations where hemoglobin was shown to leak from the cells (Fig. 6). Interestingly, NBD-PA-labeled ghosts (Figs. 9 andS6) show intense spots on the membrane where the dye appears to concentrate. Because the hemolysis assays were carried out with RBCs, whereas SS-NMR measurements were performed with labeled ghosts, we imaged the calcein influx on ghosts by fluorescence microscopy. The results (Fig. S7) not only prove that the influx in the ghost membrane is possible but also that the membrane can be crossed by molecules as large as calcein.

DISCUSSION

These results, analyzed together with those of the hemolysis assay, can be interpreted in terms of membrane perturbation mechanisms. The facts that aurein 1.2 exerts its hemolytic action at later stages than caerin 1.1, that the lipid dynamics in the hydrophobic region increase when the peptide concentration increases, and that small, rapidly reorienting objects are formed indicate a carpet-like mechanism, as schematized in Fig. 10 *A*. This mechanism is also supported by the more diffuse appearance of fluorescence-labeled ghosts, as seen by confocal fluorescence microscopy (Fig. 9).

In the case of caerin 1.1, the leakage results, ^{31}P SS-NMR spectra, and confocal microscopy images are compatible with a pore-forming mechanism (Fig. 10 *B*) where the broad isotropic contribution would result from high-curvature regions in the membrane such as those expected in a toroidal pore (63). It is also tempting to assign the bright NBD-PA fluorescence spots to pore locations, although an unambiguous explanation for the concentration of the fluorescent tag in the pores remains elusive. Nonetheless, other mechanisms have been described that cannot be ruled out (17,18). In particular, dynamic models where the membrane only transiently becomes permeable could be considered. A full proof of pore formation can only be obtained by more detailed spectroscopical measurements, which are currently underway.

^{2}H SS-NMR spectra monitor the acyl chain order profile of the PA-d_{31} molecules inserted into the ghost membrane and not of the endogenous phospholipid chains, although this "reporter" molecule is very likely to reflect the overall state of the membrane. As a result of the presence of PC, SM, and Chol in ghost membranes, liquid-ordered and liquid-disordered domains can coexist, a delicate phase equilibrium that can potentially be perturbed by addition of PA-d_{31} (64). The preferential interaction of an AMP with membrane domains of lower thickness or at domain boundaries has recently been predicted and reported

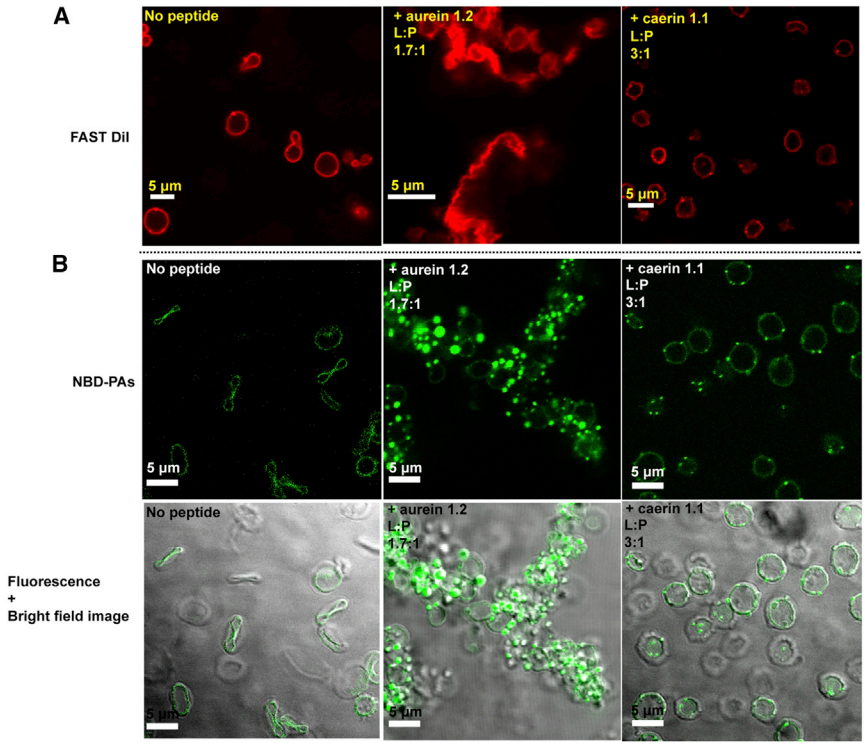

FIGURE 9 Confocal fluorescence microscopy images of ghosts. (*A*) FAST DiI entrapped in unlabeled ghosts with addition of AMPs and (*B*) NBD-PAs entrapped in deuterated ghosts with addition of AMPs. The corresponding L/P molar ratios are indicated, and the scale bars are 5 µm. To see this figure in color, go online.

(65,66). A preferential interaction of caerin with the liquid-disordered domain could expel the PA into the liquid-ordered phase or at the interface, resulting in stiffening of the rest of the membrane. This would explain the different dynamic behavior of PA-d_{31} upon caerin addition compared with aurein. It is noteworthy that the effects of AMPs observed by SS-NMR on labeled ghost membranes occur at L/P molar ratios similar to those observed in hemolytic assays on intact RBCs. We thus consider that, despite the changes in the FA chain profile because of labeling (an unavoidable drawback required to perform experiments on whole cells rather than model membranes), the mechanisms of action we elucidated are closely related to those taking place in intact RBCs.

Our results indicate that aurein 1.2 and caerin 1.1 interact with erythrocyte membranes via similar mechanisms that take place with bacterial membranes and that their relative potency is maintained (61). Both peptides have been shown to at least partially adopt an α-helical structure when interacting with membranes (59). These α helices are amphipathic with all charged and polar residues found along one side of the helix and amino acids with non-polar side chains on the opposite side (Fig. S8) (67). The interaction with the membrane results from electrostatic and hydrophobic interactions as well as from the respective shapes of lipids and peptides (18,19). The fact that the AMPs maintain similar action mechanisms on RBC and bacteria membranes despite differences in surface charge seems to indicate that hydrophobic interactions play an important role in dictating this mechanism. Electrostatic interactions are likely to play a greater role in "capture" of the AMPs, explaining their higher potency toward bacteria.

CONCLUSIONS

In this study, we took a new approach to understand the action mechanism of AMPs on erythrocyte membranes. Preparing ghosts by removing the contents of erythrocytes preserves the cell surface and membrane composition while ensuring minimal interference with ^{31}P and ^{2}H SS-NMR analysis. The successful non-biochemical labeling of erythrocyte ghost membranes with deuterated FAs opens the possibility for other types of lipid labeling, such as with ^{13}C-labeled FAs.

Using hemolysis assays and ^{31}P static and ^{2}H MAS SS-NMR, we confirmed the poor therapeutic quality of aurein 1.2 and caerin 1.1 in their current versions (56,61). Although both AMPs lyse bacteria at low concentrations, they present poor selectivity between Gram+ and Gram− bacteria, and we showed that their hemolytic potency is too high for safe use in the clinic. We also showed that higher concentrations of these peptides are required to perturb intact RBCs compared with model membranes. This may be explained by the fact that RBC membranes have not only lipids but also glycocalyx on their surface, which is rich in carbohydrates, and have many transmembrane proteins embedded. Although our experimental protocols are established to compare similar L/P ratios in erythrocytes, ghosts, and

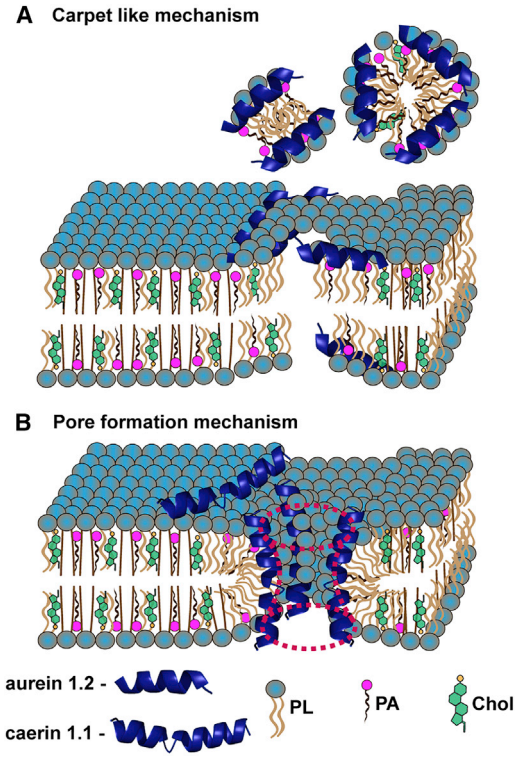

FIGURE 10 Cartoon representation of AMPs' potential action mechanisms on ghost membranes incorporating deuterated PA. (*A*) Carpet mechanism with aurein binding on the surface and then disrupting the membrane by micellization. (*B*) Pore formation by caerin after binding on the surface. To see this figure in color, go online.

model membranes, we want to stress that, in some medical cases, the ratio of bacteria to RBCs or other mammalian cells may be such that a small concentration of AMPs may be enough to kill all bacteria while leaving most mammalian cells alive.

Despite these concentration considerations, AMPs' mechanisms of interaction on RBCs are similar to those adopted in bacteria. Such a similarity may be specific to the peptides studied here because many factors need to be taken into account when comparing peptide-membrane interactions with different cell membrane types. Comparison between erythrocytes and bacteria highlights the importance of hydrophobic effects in determining the mode of peptide interaction with membranes. A detailed understanding of the interaction of AMPs with mammalian cells is an essential step for their use as therapeutic agents in the clinics and for their improvement before reaching the market. The methodology described here does not rely on cell metabolism and can, at least in principle, be transposed to other eukaryotic cells or those of other organisms.

SUPPORTING MATERIAL

Supporting material can be found online at https://doi.org/10.1016/j.bpj.2022.03.009.

AUTHOR CONTRIBUTIONS

Conceptualization, A.A.A., D.E.W., and I.M.; methodology, data collection, and initial analysis, K.K. and M.S.; additional analysis, A.A.A., D.E.W., and I.M.; original draft preparation, K.K. and A.A.A.; review and editing, S.B., A.A.A., M.S., D.E.W., and I.M.; supervision and funding acquisition, D.E.W., S.B., and I.M. All authors have read and agreed to the published version of the manuscript.

ACKNOWLEDGMENTS

This research was funded by the Natural Sciences and Engineering Research Council of Canada (NSERC) (grant RGPIN-2018–06200 to I.M.) and the Centre National de la Recherche Scientifique (UMR 7203 to D.E.W.). K.K. would like to thank the Quebec Network for Research on Protein Function, Engineering, and Applications (PROTEO) – Strategic Cluster of the Fonds de recherche du Québec – Nature et Technologies (FRQNT) for the award of a scholarship. M.S. is grateful to the NSERC for the award of a scholarship.

REFERENCES

1. World Health Organization (WHO), Global Priority List of Antibiotic-Resistant Bacteria to Guide Research, Discovery and Development of New Antibiotics. Geneva, Switzerland. 2021.
2. World Health Organization (WHO), 2014, Antimicrobial Resistance Global Report on Surveillance: 2014 Summary.
3. Koehbach, J., and D. J. Craik. 2019. The vast structural diversity of antimicrobial peptides. *Trends Pharmacol. Sci.* 40:517–528.
4. Booth, V., D. E. Warschawski, …, I. Marcotte. 2017. Recent progress on the application of ^{2}H solid-state NMR to probe the interaction of antimicrobial peptides with intact bacteria. *Biochim. Biophys. Acta Proteins Proteom.* 1865:1500–1511.
5. Yeaman, M. R., and N. Y. Yount. 2003. Mechanisms of antimicrobial peptide action and resistance. *Pharmacol. Rev.* 55:27–55.
6. Hancock, R. E., and M. G. Scott. 2000. The role of antimicrobial peptides in animal defenses. *Proc. Natl. Acad. Sci. U S A.* 97:8856–8861.
7. Mookherjee, N., M. A. Anderson, …, D. J. Davidson. 2020. Antimicrobial host defence peptides: functions and clinical potential. *Nat. Rev. Drug Discov.* 19:311–332.
8. Mor, A. 2009. Multifunctional host defense peptides: antiparasitic activities. *FEBS J.* 276:6474–6482.
9. Hoskin, D. W., and A. Ramamoorthy. 2008. Studies on anticancer activities of antimicrobial peptides. *Biochim. Biophys. Acta Biomembr.* 1778:357–375.
10. Umnyakova, E. S., M. S. Zharkova, …, V. N. Kokryakov. 2020. Human antimicrobial peptides in autoimmunity. *Autoimmunity.* 53:137–147.
11. Lambert, P. 2002. Cellular impermeability and uptake of biocides and antibiotics in Gram-positive bacteria and mycobacteria. *J. Appl. Microbiol.* 92:46S–54S.
12. Costerton, J., R. Irvin, …, I. Sutherland. 1981. The role of bacterial surface structures in pathogenesis. *CRC Crit. Rev. Microbiol.* 8:303–338.
13. Zhao, W., T. Róg, …, M. Karttunen. 2007. Atomic-scale structure and electrostatics of anionic palmitoyloleoylphosphatidylglycerol lipid bilayers with Na^{+} counterions. *Biophysical J.* 92:1114–1124.
14. Guilhelmelli, F., N. Vilela, …, C. Kyaw. 2013. Antibiotic development challenges: the various mechanisms of action of antimicrobial peptides and of bacterial resistance. *Front. Microbiol.* 4:353.
15. Schmidtchen, A., M. Pasupuleti, and M. Malmsten. 2014. Effect of hydrophobic modifications in antimicrobial peptides. *Adv. Colloid Interf. Sci.* 205:265–274.
16. Wessels, J., and J. Veerkamp. 1973. Some aspects of the osmotic lysis of erythrocytes III. Comparison of glycerol permeability and lipid

composition of red blood cell membranes from eight mammalian species. *Biochim. Biophys. Acta Biomembr.* 291:190–196.

17. Bechinger, B. 2015. The SMART model: soft Membranes Adapt and Respond, also Transiently, in the presence of antimicrobial peptides. *J. Pept. Sci.* 21:346–355.
18. Aisenbrey, C., A. Marquette, and B. Bechinger. 2019. The mechanisms of action of cationic antimicrobial peptides refined by novel concepts from biophysical investigations. *Adv. Exp. Med. Biol.* 1117:33–64.
19. Greco, I., N. Molchanova, …, J. Svenson. 2020. Correlation between hemolytic activity, cytotoxicity and systemic in vivo toxicity of synthetic antimicrobial peptides. *Sci. Rep.* 10:1–13.
20. Balla, M., J. Bowie, and F. Separovic. 2004. Solid-state NMR study of antimicrobial peptides from Australian frogs in phospholipid membranes. *Eur. Biophys. J.* 33:109–116.
21. Marcotte, I., K. L. Wegener, …, F. Separovic. 2003. Interaction of antimicrobial peptides from Australian amphibians with lipid membranes. *Chem. Phys. Lipids.* 122:107–120.
22. Bechinger, B. 1999. The structure, dynamics and orientation of antimicrobial peptides in membranes by multidimensional solid-state NMR spectroscopy. *Biochim. Biophys. Acta Biomembr.* 1462:157–183.
23. Fernandez, D. I., M.-A. Sani, …, F. Separovic. 2013. Membrane defects enhance the interaction of antimicrobial peptides, aurein 1.2 versus caerin 1.1. *Biochim. Biophys. Acta Biomembr.* 1828:1863–1872.
24. Laadhari, M., A. A. Arnold, …, I. Marcotte. 2016. Interaction of the antimicrobial peptides caerin 1.1 and aurein 1.2 with intact bacteria by ^{2}H solid-state NMR. *Biochim. Biophys. Acta.* 1858:2959–2964.
25. Arnold, A. A., J.-P. Bourgouin, …, I. Marcotte. 2018. Whole cell solid-state NMR study of Chlamydomonas reinhardtii microalgae. *J. Biomol. NMR.* 70:123–131.
26. Poulhazan, A., A. A. Arnold, …, I. Marcotte. 2018. Unambiguous ex situ and in cell 2D ^{13}C solid-state NMR characterization of starch and its constituents. *Int. J. Mol. Sci.* 19:3817.
27. Apponyi, M. A., T. L. Pukala, …, F. Separovic. 2004. Host-defence peptides of Australian anurans: structure, mechanism of action and evolutionary significance. *Peptides.* 25:1035–1054.
28. Rozek, T., K. L. Wegener, …, M. J. Tyler. 2000. The antibiotic and anticancer active aurein peptides from the Australian bell frogs Litoria aurea and Litoria raniformis: the solution structure of aurein 1.2. *Eur. J. Biochem.* 267:5330–5341.
29. Wong, H., J. H. Bowie, and J. A. Carver. 1997. The solution structure and activity of caerin 1.1, an antimicrobial peptide from the Australian green tree frog, Litoria splendida. *Eur. J. Biochem.* 247:545–557.
30. Wegener, K. L., C. S. Brinkworth, …, M. J. Tyler. 2001. Bioactive dahlein peptides from the skin secretions of the Australian aquatic frog Litoria dahlii: sequence determination by electrospray mass spectrometry. *Rapid Commun. Mass Spectrom.* 15:1726–1734.
31. Dodge, J. T., C. Mitchell, and D. J. Hanahan. 1963. The preparation and chemical characteristics of hemoglobin-free ghosts of human erythrocytes. *Arch. Biochem. Biophys.* 100:119–130.
32. Schwoch, G., and H. Passow. 1973. Preparation and properties of human erythrocyte ghosts. *Mol. Cell. Biochem.* 2:197–218.
33. Maraviglia, B., J. H. Davis, …, K. W. Wirtz. 1982. Human erythrocyte membranes are fluid down to− 5° C. *Biochim. Biophys. Acta Biomembr.* 686:137–140.
34. Davis, J. H., B. Maraviglia, …, D. V. Godin. 1979. Bilayer rigidity of the erythrocyte membrane ^{2}H-NMR of a perdeuterated palmitic acid probe. *Biochim. Biophys. Acta Biomembr.* 550:362–366.
35. Preté, P. S., C. C. Domingues, …, S. Schreier. 2011. Multiple stages of detergent-erythrocyte membrane interaction—a spin label study. *Biochim. Biophys. Acta Biomembr.* 1808:164–170.
36. Warschawski, D. E., A. A. Arnold, and I. Marcotte. 2018. A new method of assessing lipid mixtures by ^{31}P magic-angle spinning NMR. *Biophysical J.* 114:1368–1376.
37. Laydevant, F., M. Mahabadi, …, D. E. Warschawski. 2021. Growth-phase dependence of bacterial membrane lipid profile and labeling for in-cell solid-state NMR applications. *Biochim. Biophys. Acta Biomembr.* 1864:183819.
38. Pernet, F., and R. Tremblay. 2003. Effect of ultrasonication and grinding on the determination of lipid class content of microalgae harvested on filters. *Lipids.* 38:1191–1195.
39. Balsgart, N. M., M. Mulbjerg, …, T. Vosegaard. 2016. High throughput identification and quantification of phospholipids in complex mixtures. *Anal. Chem.* 88:2170–2176.
40. Rance, M., and R. A. Byrd. 1983. Obtaining high-fidelity spin-12 powder spectra in anisotropic media: phase-cycled Hahn echo spectroscopy. *J. Magn. Reson.* 52:221–240.
41. Warnet, X. L., M. Laadhari, …, D. E. Warschawski. 2016. A ^{2}H magic-angle spinning solid-state NMR characterisation of lipid membranes in intact bacteria. *Biochim. Biophys. Acta Biomembr.* 1858:146–152.
42. Burnett, L., and B. Muller. 1971. Deuteron quadrupole coupling constants in three solid deuterated paraffin hydrocarbons: C_2D_6, C_4D_{10}, C_6D_{14}. *J. Chem. Phys.* 55:5829–5831.
43. Moroi, Y. 1992. Micelles: Theoretical and Applied Aspects. Springer Science & Business Media, Plenum Press, New York and London.
44. Patist, A., J. R. Kanicky, …, D. O. Shah. 2002. Importance of micellar kinetics in relation to technological processes. *J. Colloid Interf. Sci.* 245:1–15.
45. Ollivon, M., S. Lesieur, …, M. t. Paternostre. 2000. Vesicle reconstitution from lipid–detergent mixed micelles. *Biochim. Biophys. Acta Biomembr.* 1508:34–50.
46. Høyrup, P., J. Davidsen, and K. Jørgensen. 2001. Lipid membrane partitioning of lysolipids and fatty acids: effects of membrane phase structure and detergent chain length. *J. Phys. Chem. B.* 105:2649–2657.
47. Heerklotz, H., and J. Seelig. 2000. Correlation of membrane/water partition coefficients of detergents with the critical micelle concentration. *Biophysical J.* 78:2435–2440.
48. Koley, D., and A. J. Bard. 2010. Triton X-100 concentration effects on membrane permeability of a single HeLa cell by scanning electrochemical microscopy (SECM). *Proc. Natl. Acad. Sci. U S A.* 107:16783–16787.
49. Yan, X., K. Kumar, …, E. Boisselier. 2021. Interactions between the cell membrane repair protein S100A10 and phospholipid monolayers and bilayers. *Langmuir.* 37:9652–9663.
50. Ijare, O. B., D. S. Baskin, and K. Pichumani. 2019. Ex Vivo ^{1}H NMR study of pituitary adenomas to differentiate various immunohistochemical subtypes. *Sci. Rep.* 9:3007.
51. MacKenzie, A., M. Vyssotski, and E. Nekrasov. 2009. Quantitative analysis of dairy phospholipids by ^{31}P NMR. *J. Am. Oil Chem. Soc.* 86:757–763.
52. Nouri-Sorkhabi, M. H., N. S. Agar, …, P. W. Kuchel. 1996. Phospholipid composition of erythrocyte membranes and plasma of mammalian blood including Australian marsupials; quantitative ^{31}P NMR analysis using detergent. *Comp. Biochem. Physiol. B Biochem. Mol. Biol.* 113:221–227.
53. Bouhlel, Z., A. A. Arnold, …, I. Marcotte. 2019. Labelling strategy and membrane characterization of marine bacteria Vibrio splendidus by in vivo ^{2}H NMR. *Biochim. Biophys. Acta Biomembr.* 1861:871–878.
54. Tardy-Laporte, C., A. A. Arnold, …, I. Marcotte. 2013. A ^{2}H solid-state NMR study of the effect of antimicrobial agents on intact Escherichia coli without mutating. *Biochim. Biophys. Acta Biomembr.* 1828:614–622.
55. Magana, M., M. Pushpanathan, …, A. L. Ferguson. 2020. The value of antimicrobial peptides in the age of resistance. *Lancet Infect. Dis.* 20:e216–e230.
56. Brian Chia, C., Y. Gong, …, M. A. Cooper. 2011. Membrane binding and perturbation studies of the antimicrobial peptides caerin, citropin, and maculatin. *Pept. Sci.* 96:147–157.
57. Lorenzon, E., P. Sanches, …, E. M. Cilli. 2013. Dimerization of aurein 1.2: effects in structure, antimicrobial activity and aggregation of Candida albicans cells. *Amino Acids.* 44:1521–1528.

58. Ramezanzadeh, M., N. Saeedi, …, A. Rezaei. 2021. Design and characterization of new antimicrobial peptides derived from aurein 1.2 with enhanced antibacterial activity. *Biochimie.* 181:42–51.

59. Sani, M.-A., S. Carne, …, F. Separovic. 2017. One pathogen two stones: are Australian tree frog antimicrobial peptides synergistic against human pathogens? *Eur. Biophys. J.* 46:639–646.

60. Fernandez, D. I., A. P. Le Brun, …, F. Separovic. 2012. The antimicrobial peptide aurein 1.2 disrupts model membranes via the carpet mechanism. *Phys. Chem. Chem. Phys.* 14:15739–15751.

61. Fernandez, D. I., J. D. Gehman, and F. Separovic. 2009. Membrane interactions of antimicrobial peptides from Australian frogs. *Biochim. Biophys. Acta Biomembr.* 1788:1630–1638.

62. Yang, Y., H. Yao, and M. Hong. 2015. Distinguishing bicontinuous lipid cubic phases from isotropic membrane morphologies using ^{31}P solid-state NMR spectroscopy. *J. Phys. Chem. B.* 119:4993–5001.

63. Li, J., J.-J. Koh, …, R. W. Beuerman. 2017. Membrane active antimicrobial peptides: translating mechanistic insights to design. *Front. Neurosci.* 11:73.

64. Shimokawa, N., R. Mukai, …, M. Takagi. 2017. Formation of modulated phases and domain rigidification in fatty acid-containing lipid membranes. *Phys. Chem. Chem. Phys.* 19:13252–13263.

65. Lee, T.-H., V. Hofferek, …, M.-I. Aguilar. 2021. The impact of antibacterial peptides on bacterial lipid membranes depends on stage of growth. *Faraday Discuss.* 232:399–418.

66. Pinigin, K. V., T. R. Galimzyanov, and S. A. Akimov. 2021. Amphipathic peptides impede lipid domain fusion in phase-separated membranes. *Membranes.* 11:797.

67. Gautier, R., D. Douguet, …, G. Drin. 2008. HELIQUEST: a web server to screen sequences with specific α-helical properties. *Bioinformatics.* 24:2101–2102.

Biophysical Journal, Volume *121*

Supplemental information

In situ solid-state NMR study of antimicrobial peptide interactions with erythrocyte membranes

Kiran Kumar, Mathew Sebastiao, Alexandre A. Arnold, Steve Bourgault, Dror E. Warschawski, and Isabelle Marcotte

Supplementary information for:

IN SITU SOLID-STATE NMR STUDY OF ANTIMICROBIAL PEPTIDE INTERACTIONS WITH ERYTHROCYTE MEMBRANES

Kiran Kumar[1,2], Mathew Sebastiao[1,2], Alexandre A. Arnold[1,2], Steve Bourgault[1,2], Dror E. Warschawski[1,3*] & Isabelle Marcotte[1,2*]

[1] Department of Chemistry, Université du Québec à Montréal, P.O. Box 8888, Downtown Station, Montreal, Canada H3C 3P8

[2] Quebec Network for Research on Protein Function, Engineering and Applications (PROTEO), Québec, Canada

[3] Laboratoire des Biomolécules, LBM, CNRS UMR 7203, Sorbonne Université, École normale supérieure, PSL University, 75005 Paris, France

*Corresponding authors:

Isabelle Marcotte
Tel: 1-514-987-3000 #5015
Fax: 1-514-987-4054
E-mail: marcotte.isabelle@uqam.ca

Dror E. Warschawski
Tel : +33 1 44 27 32 16
Fax : +33 1 44 27 62 50
E-mail: Dror.Warschawski@Sorbonne-Universite.fr

Lipid concentration

To determine the final lipid concentration in the NMR or leakage assay samples, and therefore determine lipid-to-peptide (L/P) ratios, the amount of lipids as a function of starting RBCs or ghosts volume needs to be determined. This was carried out using ^{31}P NMR and the well-resolved PC peak at -0.81 ppm present in all samples.

In brief, the integral of the PC ^{31}P NMR peak as a function of RBC (or ghost) sample volume was plotted, as seen in Fig. S1A. Since RBCs (or ghosts) are composed of 33 % PC, the final total lipid concentration in the sample is obtained by multiplying the determined concentration by three.

The corresponding integrals were related to PC concentrations using a calibration curve determined with solutions of DOPC at various known concentrations (Fig. S1B). The obtained lipid concentration can be converted into lipid weight, by using an average molecular weight:

$$w_n = \sum_i^n w_i x_i$$

Where w_i is the molecular weight of each lipid molecule and x_i is the molar fraction of each lipid (headgroups determined by ^{31}P NMR and acyl chain lengths determined by GCMS). In the case of ghosts, the average molecular weight is 735 g/mol. The conversion of Fig. S1A from concentration to weight is shown in Fig. S1C.

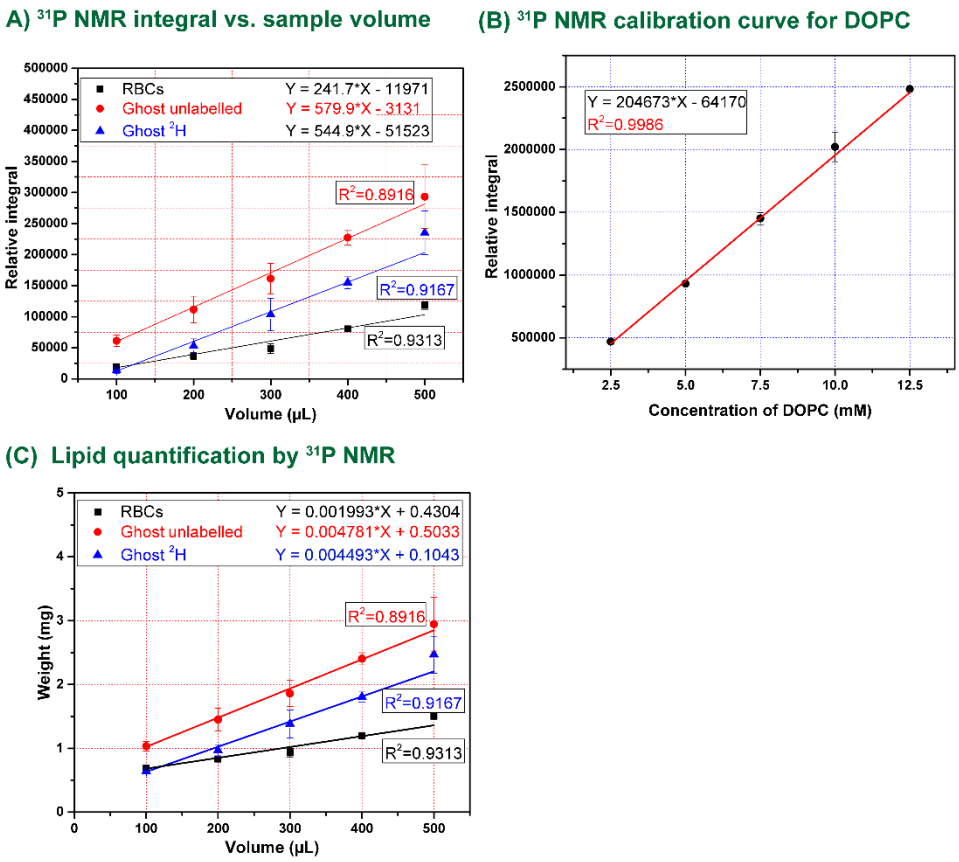

Figure S1: (A) Integral of the PC ^{31}P NMR peak as a function of RBC (or ghost) sample volume. **(B)** Integral of the PC ^{31}P NMR peak as a function of DOPC concentration. **(C)** RBC (or ghost) lipid weight as a function of sample volume.

Lipid profile and chemical shifts

We have identified and quantified the phospholipids (PLs) in RBCs, unlabeled ghosts and deuterated ghosts samples after performing lipid extraction, ^{31}P 1D, ^{1}H 1D and ^{31}P-^{1}H 2D solution NMR experiments, as well as GCMS on hydrolyzed fatty acids (FAs). Figure S2 contains the overlay of ^{1}H and ^{31}P NMR spectra.

All chemical shifts have been determined from the 2D spectra, except for the γ protons of PC and SM, determined from ^{1}H 1D spectra, and the γ protons of PCe and DHSM, which have been interpolated.

Numerical results, including ^{1}H and ^{31}P chemical shifts, lipid classes and FA abundances, are presented in Tables S1 and S2, as the mean of triplicate measurements.

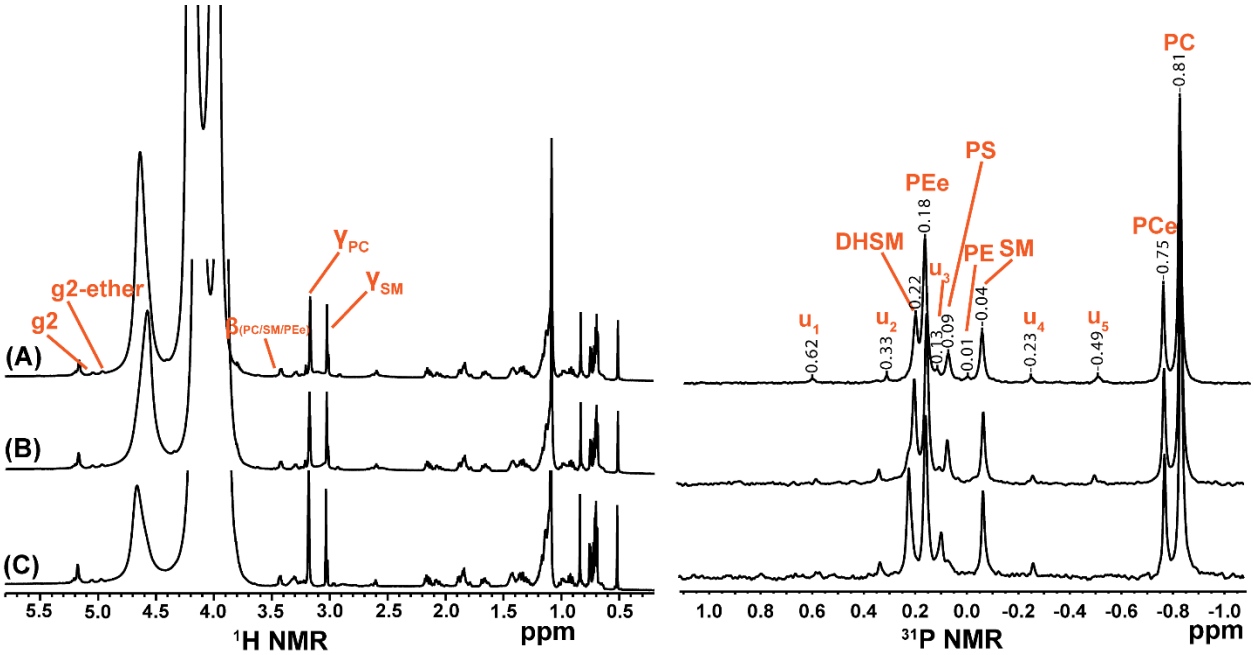

Figure S2: ^{1}H- and ^{31}P-NMR spectra of (A) unlabeled ghost PLs, (B) deuterated ghosts PLs and (C) RBCs membrane PLs. All spectra were acquired at 298 K, and "u" indicates unassigned peaks.

Table S1: Distribution (%) of phospholipids in horse RBC membranes as determined by ^{1}H- and ^{31}P solution NMR, with ^{31}P and ^{1}H chemical shifts. Standard deviations are indicated.

PLs	Chemical shift (ppm)		Abundance (%)		
	^{31}P	^{1}H	RBCs	Unlabeled ghosts	^{2}H ghosts
PC	-0.81	α: 4.08 β: 3.43 γ: 3.18 g1: 3.98, 4.23 g2: 5.05 g3: 3.80	34.8 (1.1)	34.1 (1.3)	34.2 (0.9)
PCe	-0.75	α: 4.07 β: 3.42 γ: ~3.2 g1, g3: 3.79 g2: 4.97	9.6 (2.1)	8.8 (0.7)	9.3 (0.9)
PE	0.01	-	-	1.9 (0.6)	1.3 (1.2)
PEe	0.18	α: 2.93 β: 3.43 g1: 3.83 g2: 4.97 g3: 3.78	22.0 (2.8)	21.6 (2.7)	19.7 (1.0)
PS	0.09	α: 4.08 β: 3.80 g1: 4.23 g2: 5.04 g3: 3.97	4.4 (1.9)	5.5 (1.4)	7.1 (2.0)
SM	-0.04	α: 4.08 β: 3.42 γ: 3.03 -CHNH-: 3.95 -$POCH_2$-: 3.73	9.9 (1.1)	9.5 (1.0)	9.1 (0.6)
DHSM	0.22	α: 4.07 β: 3.44 γ: ~3.0 -CHNH-: 3.96 -$POCH_2$-: 3.78	14.4 (0.5)	12.6 (2.6)	13.6 (2.4)
Others	-		4.9 (0.7)	6.1 (1.9)	5.7 (1.5)

Table S2: Distribution (%) of total fatty acids in horse RBCs membranes as determined by GCMS. Standard deviations are indicated.

FAs	Abundance (%)		
	RBCs	Unlabeled ghosts	^{2}H ghosts
C16:0 ^{2}H	-	-	25.2 (1.5)
C16:0	27.6 (0.7)	24.4 (0.7)	20.1 (0.1)
18:0	27.4 (0.5)	29.3 (1.5)	19.2 (2.7)
C18:1	22.1 (0.3)	20.4 (0.6)	15.8 (0.1)
C18:2	22.9 (1.5)	25.9 (2.8)	19.7 (4.2)

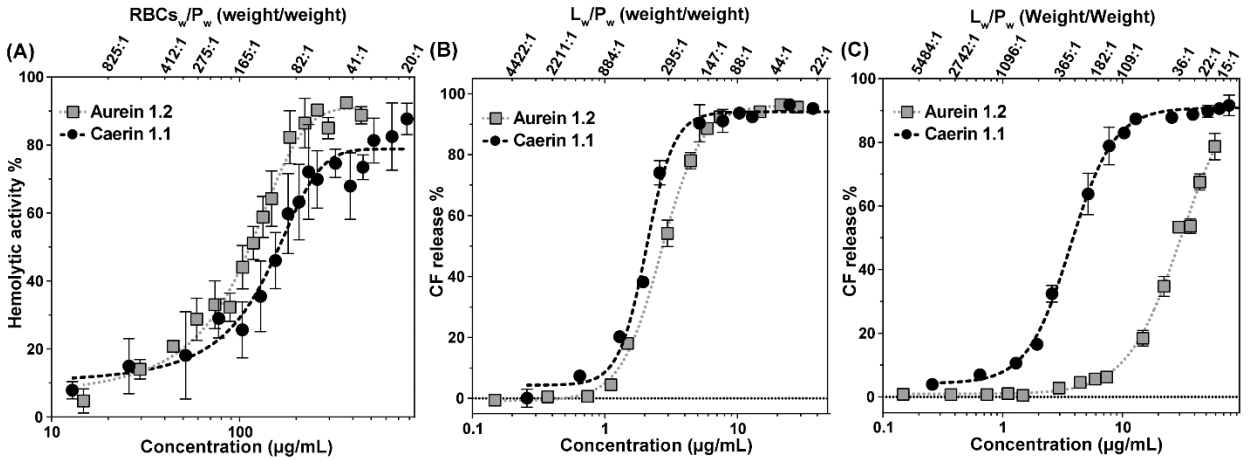

Figure S3. Lytic activity of antimicrobial peptides on erythrocytes and model membranes as determined by **(A)** hemoglobin leakage of RBCs with a phospholipid concentration of 200 µM, **(B)** carboxyfluorescein leakage of POPC/SM/Chol LUVs with a lipid concentration of 100 µM and **(C)** carboxyfluorescein leakage of POPE/POPG with a lipid concentration of 150 µM. Results are presented as the mean of triplicate assays. Dashed and dotted lines correspond to the best fit to a sigmoidal curve. All data are reported as a function of RBC or lipid-to-peptide weights. Data as a function of lipid-to-peptide molar ratios are shown in Figure 6 of the article.

Additional ^{31}P NMR spectra

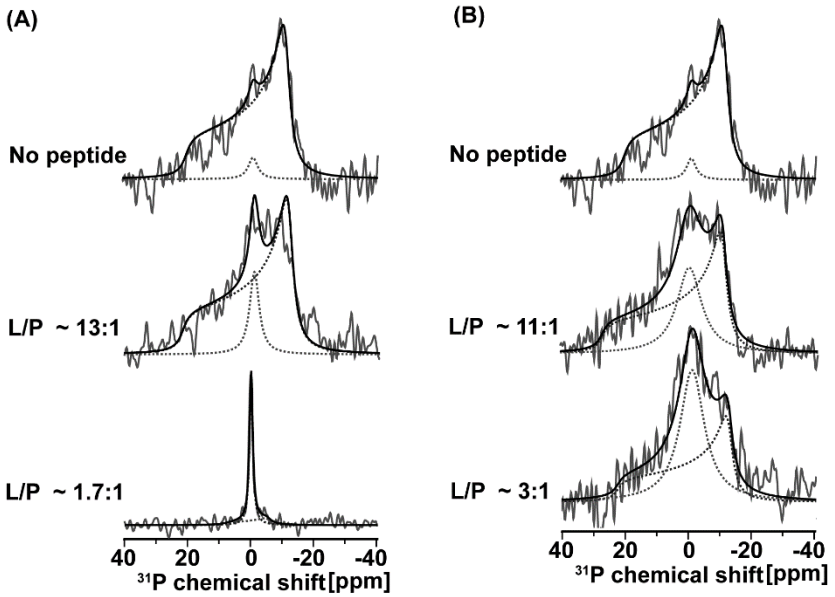

Figure S4: ^{31}P static SS-NMR spectra of deuterated ghosts, acquired at 293 K with the addition of different concentrations of **(A)** aurein 1.2 and **(B)** caerin 1.1. The corresponding lipid-to-peptide molar ratios (L/P) are indicated. Dotted lines represent spectral fitting of the anisotropic components and the isotropic peak.

Table S3: ^{31}P NMR isotropic contribution (%) for unlabeled and deuterated ghosts with different concentrations of peptides. Standard deviations are indicated.

Aurein 1.2				Caerin 1.1			
Unlabeled ghosts		Deuterated ghosts		Unlabeled ghosts		Deuterated ghosts	
L/P	Isotropic contribution (%)	L/P	Isotropic contribution (%)	L/P	Isotropic contribution (%)	L/P	Isotropic contribution (%)
-	8.3 (2.1)	-	4.1 (0.3)	-	8.3 (2.1)	-	4.1 (0.3)
13:1	16.3 (2.9)	13:1	18.9 (7.8)	22:1	22.3 (0.1)	-	-
6:1	28.0 (5.0)	6:1	28.8 (2.5)	11:1	29.0 (1.0)	11:1	34.2 (1.5)
4:1	43.8 (0.1)	-	-	8:1	32.3 (1.5)	-	-
3:1	43.9 (1.2)	-	-	5:1	33.6 (0.2)	-	-
2:1	65.0 (0.3)	-	-	3:1	47.1 (3.3)	3:1	58.4 (7.8)
1.7:1	79.9 (0.1)	1.7:1	78.2 (3.5)				

Table S4. Effect of the antimicrobial peptides on the second spectral moment, M_2, from the ^2H SS-NMR MAS spectra, as well as ^{31}P CSA with standard deviation, as a function of the lipid-to-peptide molar ratio (L/P). ^{31}P and ^2H SS-NMR data were obtained with unlabeled and deuterated ghosts, respectively.

Aurein 1.2			Caerin 1.1		
L/P	M_2 (10^9 rad. s^{-2})	CSA (ppm)	L/P	M_2 (10^9 rad. s^{-2})	CSA (ppm)
-	9.9 (0.5)	26.1 (0.2)	-	9.9 (0.5)	26.1 (0.2)
13:1	8.2 (0.5)	23.2 (4.7)	22:1	10.8 (0.2)	25.2 (0.9)
6:1	7.3 (0.1)	26.2 (2.2)	11:1	11.3 (1.1)	23.9 (2.5)
4:1	5.1 (0.8)	25.9 (2.4)	8:1	10.0 (1.1)	24.5 (0.5)
3:1	3.8 (0.0)	25.9 (1.6)	5:1	9.8 (0.8)	23.7 (0.1)
2:1	2.5 (0.1)	24.5 (0.7)	3:1	9.9 (1.3)	22.1 (2.1)
1.7:1	1.2 (0.3)	7.4 (3.6)			

Additional confocal fluorescence microscopy images

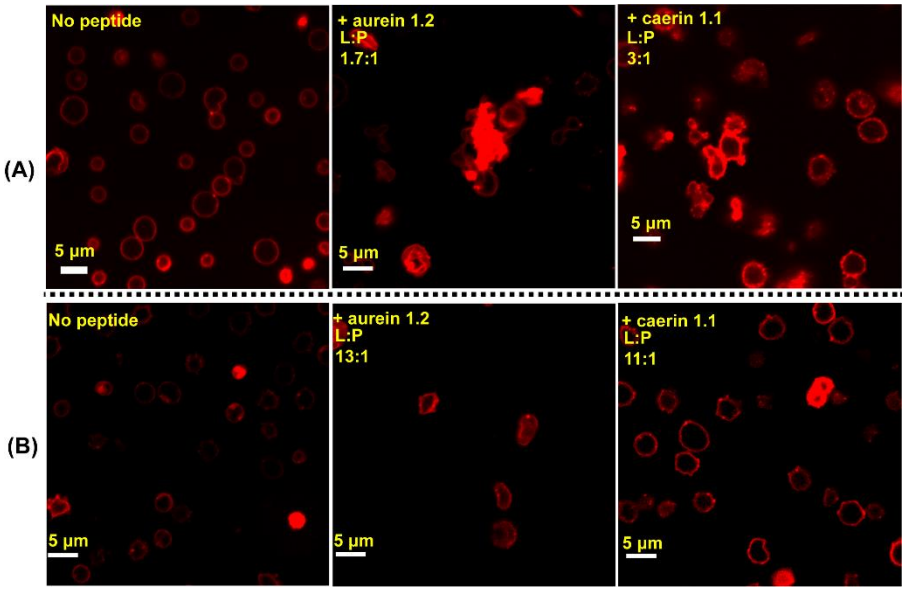

Figure S5: Confocal image of the fluorescence of Fast DiI entrapped in **(A)** deuterated ghosts and **(B)** unlabeled ghosts with different concentrations of aurein 1.2 and caerin 1.1.

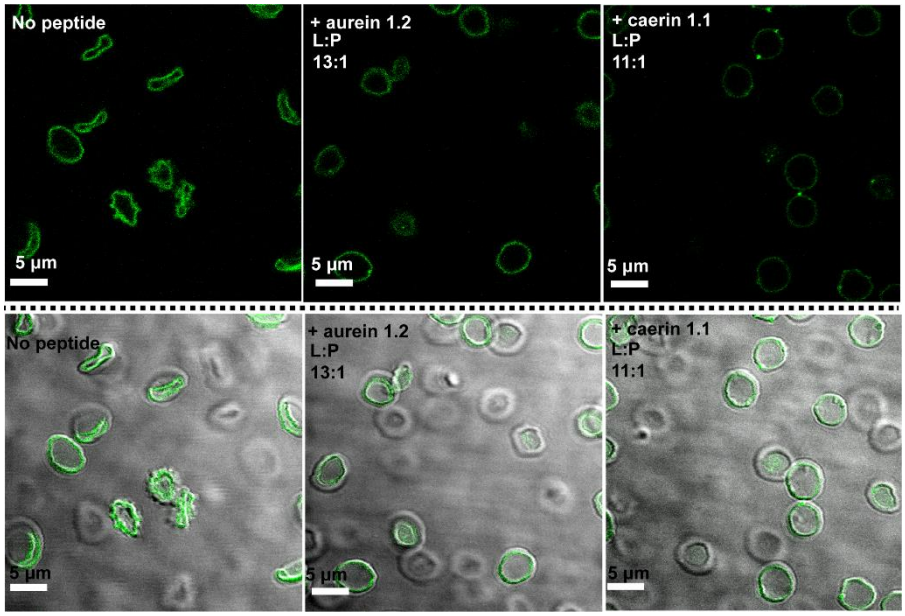

Figure S6: Confocal image of the fluorescence of NBD-PAs entrapped in deuterated ghosts with different concentrations of aurein 1.2 and caerin 1.1.

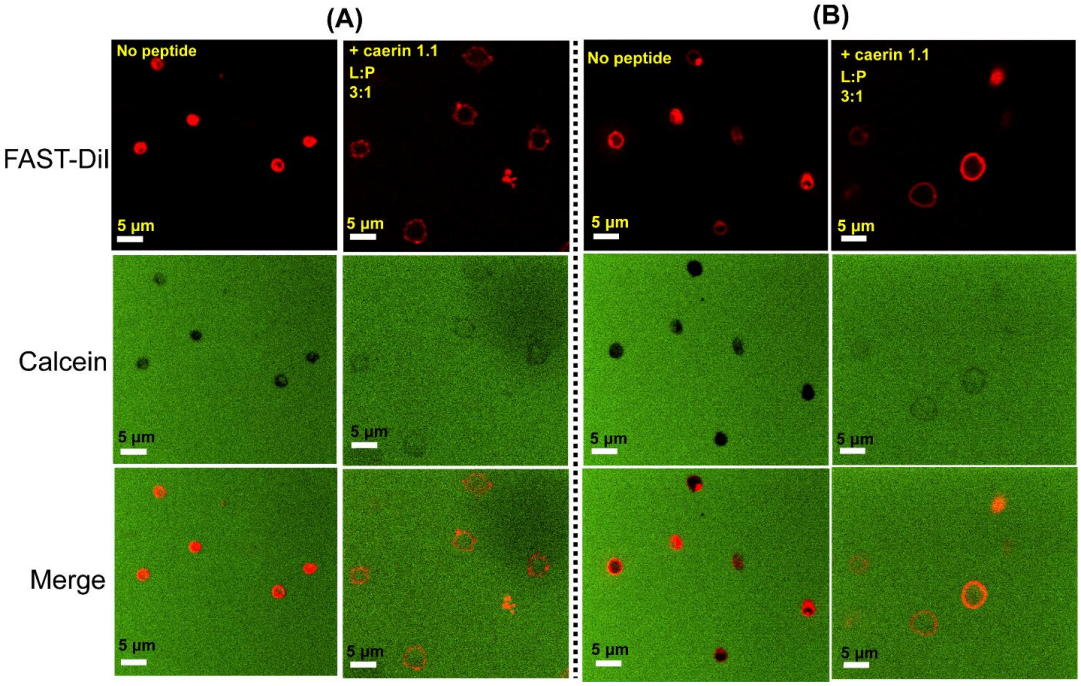

Figure S7: Confocal fluorescence microscopy image of FAST DiI entrapped in the ghost membrane pool and calcein leakage experiments of **(A)** unlabeled ghosts and **(B)** deuterated ghosts with addition of AMPs

Helical wheel representations of AMPs

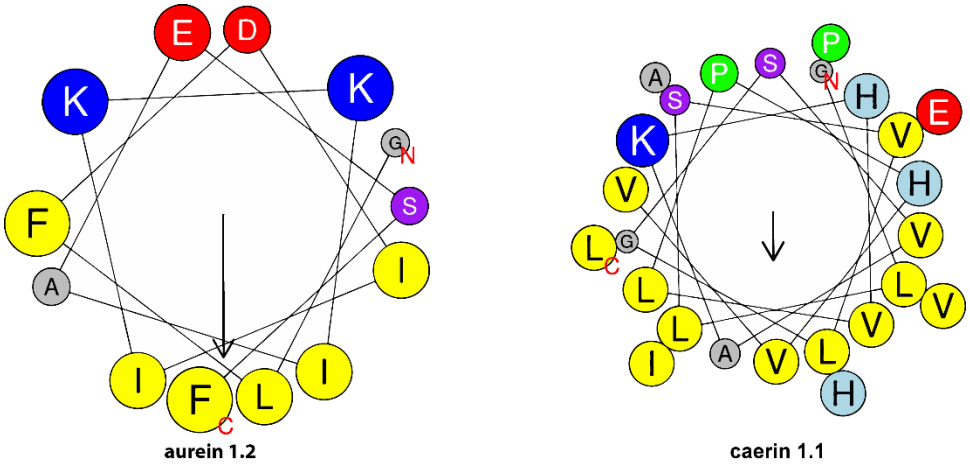

Figure S8: Helical wheel representations of aurein 1.2 (left) and caerin 1.1 (right), showing their amphiphilicity (https://heliquest.ipmc.cnrs.fr).